Robotica (2022), **40**, pp. 2168–2188
doi:10.1017/S0263574721001594

CAMBRIDGE
UNIVERSITY PRESS

RESEARCH ARTICLE

Rigid–flexible coupling dynamics analysis with joint clearance for a 5-DOF hybrid polishing robot

Feng Guo, Gang Cheng*, Shilin Wang and Jun Li

School of Mechatronic Engineering, China University of Mining and Technology, Xuzhou, China
*Corresponding author. E-mail: chg@cumt.edu.cn

Received: 8 August 2021; **Revised:** 23 September 2021; **Accepted:** 12 October 2021;
First published online: 2 December 2021

Keywords: hybrid polishing robot, rigid–flexible coupling dynamics, equivalent load, branched-chain elasticity, joint clearance

SUMMARY

Considering the polishing requirements for high-precision aspherical optical mirrors, a hybrid polishing robot composed of a serial–parallel manipulator and a dual rotor grinding system is proposed. Firstly, based on the kinematics of serial components, the equivalent load model for the parallel manipulator is established. Then, the elastodynamic model of kinematic branched-chains of the parallel manipulator is established by using the spatial beam element, and the rigid–flexible coupling dynamic model of the polishing robot is obtained with Kineto-elasto dynamics theory. Further, considering the dynamic properties of the joint clearance, the rigid–flexible coupling dynamic model with the joint clearance for the polishing robot is established. Finally, the equivalent load distribution of the parallel manipulator is analyzed, and the effect of the branched-chain elasticity and joint clearance on the motion error of the polishing robot is studied. This article provides a theoretical basis for improving the motion accuracy and dynamic performance of the hybrid polishing robot.

1. Introduction

Large aperture and high precision optical mirrors put forward higher requirements for optical processing equipment, and the traditional polishing equipment mainly adopts a gantry structure, which has the problems of the huge structure, poor flexibility, and high cost. With the advantages of high flexibility, low cost, and multiple assistance, industrial robots have been introduced into the fields of manufacturing and motion simulation [1–3]. Further, compared with the serial mechanism, the parallel manipulator (PM) has the advantages of high stiffness, high precision, and high bearing capacity, which is widely used for many fields [4, 5].

Parallel or hybrid robots for polishing operations are required to drive the grinding system to traverse every point of the mirror surface and adjust the motion attitude in real time. Therefore, the robot needs high dynamic performance and motion accuracy. Lin et al. [6] developed a five degrees of freedom (5-DOF) hybrid polishing machine and studied the dynamics and control performance. Xu et al. [7] designed a serial–parallel polishing machine for polishing the free-form surface. In addition, a single PM cannot meet the machining need of large-scale parts due to the limitation of the motion workspace, and multiple robots have to be used for collaborative processing. Meanwhile, researchers have developed a hybrid robot, which consists of a rotating module connected to a PM and can achieve five or six degrees of freedom in the workspace [8, 9]. Besides, the PM consists of several kinematic branched-chains and various motion joints, the elastic deformation of the motion components, the clearance, friction, and contact deformation for the motion joints will affect the dynamic characteristics and motion accuracy of the robot [10, 11]. A lot of studies have been carried out on the optimization of structure and control parameters [12, 13], motion coupling control [14], disturbance suppression or compensation [15, 16] for PMs. Dynamic modeling methods for PMs include Newton–Euler method, Lagrange method, virtual

work principle method, and Kane method [17–20]. Dong et al. [21] present a semi-analytical approach for elastodynamic modeling of Tricept robot based on the screw theory and combined with the dual properties of twist/wrench systems and a static condensation technique. For the elastodynamic of fully flexible parallel robots, Cammarata provided a novel derivation of the Cartesian stiffness and inertia matrices for PMs, the proposed method allows for obtaining consistent Cartesian matrices at different nodes of interest without redefining the transformation matrices typical of the Jacobian-based methods [22]. Alessandro et al. [23] performed the elastodynamic optimization of a 3T1R PM and based on the fixed pose optimization and the global optimization inside a cube, the first natural frequency and its distribution within the robots constant orientation workspace are analyzed. Most researchers usually regard the motion joint as the ideal joint. When the clearance of the motion joint is considered, the clearance can be simplified as fixed assembly clearance [24] or irregular clearance caused by wear in practice [25]. However, due to the complexity of the irregular clearance caused by the wear of the moving pair, many studies are focused on the fixed assembly clearance [26]. The existence of the clearance of the motion joint will cause a collision in the motion joint. Chen et al. [27] deduced the nonlinear dynamics equation for 4UPS-RPU PM with spherical clearance by Lagrange method. Based on elastic Hertz theory with a dissipative term, Varedi-Koulaei et al. used a continuous contact force model to evaluate the contact force and analyzed the effects of working speed and clearance size on the dynamic characteristics of a planar mechanical system [28]. Xu et al. introduced an improved impact force model and a modified friction force model to evaluate the effects of impact and friction in the clearance joints for a planar PM which has two clearance joints in the left wing and right wing [29]. When a parallel or hybrid robot is applied to large optical mirror polishing, it is necessary to establish a rigid–flexible coupling dynamic model to analyze the distribution characteristics of the robot's load and motion errors and to consider the influence of the joint effects for improving the dynamic performance and motion accuracy of the polishing robot. In addition, the rigid–flexible coupling dynamics analysis considering the joint clearance also provides the basis for the optimization of structural parameters and the design of control strategies for the polishing robot.

The rest of this article is organized as follows. In Section 2, the structure and coordinate systems of the polishing robot are introduced. In Section 3, the kinematic and dynamic models of the serial component of the polishing robot are established. In Section 4, the rigid–flexible coupling dynamic model of the PM for the polishing robot is established considering the elastic deformation of kinematic branched-chains. In Section 5, considering the influence of the joint clearance, the rigid–flexible coupling dynamic model with the joint clearance is further obtained. In Section 6, the equivalent load distribution of the serial component on the PM is analyzed, and the effect of branch-chains elasticity and joint clearance on the motion error of the moving platform is studied.

2. Description and Coordinate Systems of Polishing Robot

The hybrid polishing robot is composed of a 3UPS/UP PM and a serial component consisting of 2R series rotary joints and a dual rotor grinding system. The structure and topology of the hybrid polishing robot are shown in Fig. 1(a) and (b). The 3UPS/UP PM consists of a static platform, a moving platform, three UPS branched-chains with the same structure, and a UP branched-chain. The UPS branched-chain is connected to the moving platform with a composite spherical joint and to the static platform with a Hooke joint, points A_i and B_i ($i = 1, 2, 3$) are the center points of the rotating shaft for the composite spherical joint and Hooke joint. Besides, the composite spherical joint can be seen as a combination of a rotating joint and a Hooke joint, and point D_i is the connection point of the rotating joint for the composite spherical joint. The UP branched-chain is fixed to the moving platform and connected to the static platform by a Hooke joint and point B is the center point of the rotating shaft for the Hooke joint. 2R series rotary joints are divided into the first joint and the second joint. The PM and 2R series rotary joints move in concert during the mirror polishing process, which can meet the 5-DOF motion demand of the grinding system in the workspace.

https://doi.org/10.1017/S0263574721001594 Published online by Cambridge University Press

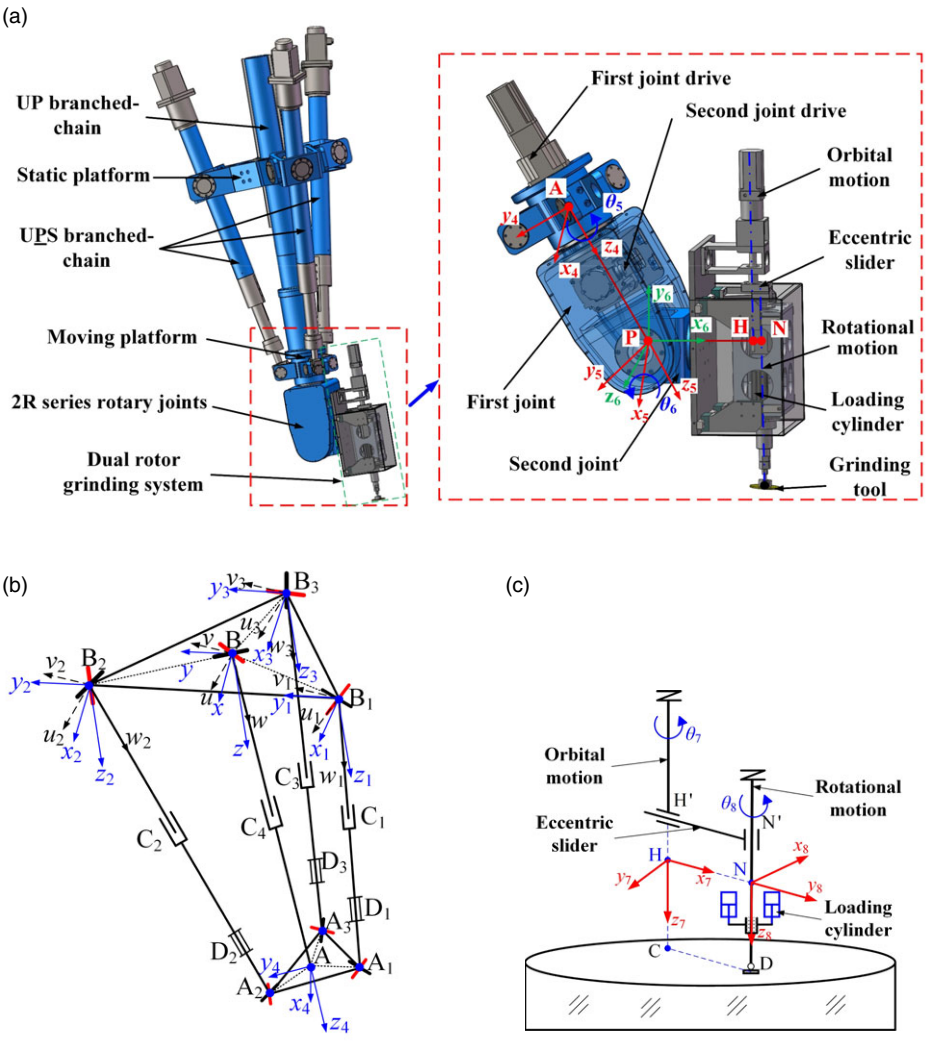

Figure 1. *Hybrid polishing robot: (a) CAD model, (b) topology, (c) diagram of dual rotor grinding system.*

In the process of large-scale optical mirror polishing, the removal function needs to be closer to the Gauss function to get better surface convergence. Thus, a planetary dual rotor grinding system is designed based on a combination of orbital and rotational motions of a small grinding tool, and the diagram of the grinding system is shown in Fig. 1(c). The orbital motor of the grinding system drives the rotation of the eccentric slider, which is fixed at one end to the orbital frame with two sets of vertical arrangement rails. The rotational motor is located in the orbital frame and drives the grinding tool with a pneumatic pressure system to complete the mirror processing. In addition, the size of the grinding tool can be adjusted to suit different polishing requirements.

Based on the right-hand rule, the base coordinate system {B-xyz} is established at point B, x-axis passes through the midpoint of B_1B_2, and z-axis is perpendicular to the static platform. The conjoined coordinate system {A-$x_4y_4z_4$} of the UP branched-chain and moving platform are established at point A, x_4-axis passes through the midpoint of A_1A_2, z_4-axis along the axis of UP branched-chain. The reference coordinate system {B_i-$x_iy_iz_i$} ($i = 1, 2, 3$) and the conjoined coordinate system {B_i-$u_iv_iw_i$} for UPS branched-chain $B_iC_iD_iA_i$ are established at point B_i, x_i-axis and z_i-axis are parallel to x-axis and z-axis, respectively, v_i-axis coincides with the axis of the far frame of UPS branched-chain Hooke joint,

https://doi.org/10.1017/S0263574721001594 Published online by Cambridge University Press

Table I. *D-H parameters of serial component.*

i	α_{i-1}	a_{i-1}	d	θ_i
5	0	0	d_4	θ_5
6	$\pi/2$	0	0	θ_6
7	$-\pi/2$	a_6	0	θ_7
8	0	0	d_7	θ_8

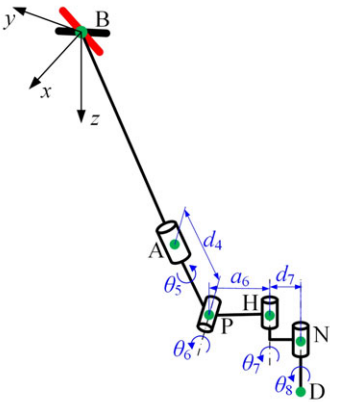

Figure 2. *Motion diagram of serial component.*

w_i-axis along the axis of UPS branched-chain. For the serial component, the conjoined coordinate system {P-$x_5y_5z_5$} of the first joint and conjoined coordinate system {P-$x_6y_6z_6$} of the second joint are established at point P, which is the intersection of rotation axes of the first joint and the second joint, y_5-axis along the rotation axis of the second joint, z_5-axis coincides with the rotation axis of the first joint, z_6-axis coincides with y_5-axis and has the same direction, and x_6-axis coincides with the installation axis of the supporting part of the grinding system. The conjoined coordinate system {H-$x_7y_7z_7$} of the orbital motion component is established at point H, which is the intersection point of the orbital motion axis and x_6-axis, z_7-axis coincides with the orbital motion axis, and x_7-axis is parallel to the offset direction of the eccentric slider. The conjoined coordinate system {N-$x_8y_8z_8$} is established at point N, which is the intersection point of the rotational motion axis and x_7-axis, z_8-axis coincides with the rotational motion axis, and x_8-axis and y_7-axis are parallel and opposite.

3. Dynamic Model of Serial Component of Polishing Robot

The serial component of the hybrid polishing robot consists of 2R series rotary joints and a dual rotor grinding system, and the kinematics can be analyzed with D-H method. The motion diagram of the serial component is shown in Fig. 2. Combined with Fig. 1, the motion parameters of the serial component are shown in Table I.

The motion parameters of 2R series rotary joints and dual rotor grinding system are measured in the conjoined coordinate system {A-$x_4y_4z_4$}, and we can obtain:

$$\begin{cases} {}^4_5\boldsymbol{T} = \begin{bmatrix} {}^4_5\boldsymbol{R} & \boldsymbol{n}_{54} \\ 0 & 1 \end{bmatrix} \\ {}^4_6\boldsymbol{T} = {}^4_5\boldsymbol{T}{}^5_6\boldsymbol{T} = \begin{bmatrix} {}^4_6\boldsymbol{R} & \boldsymbol{n}_{64} \\ 0 & 1 \end{bmatrix} \end{cases}, \quad \begin{cases} {}^4_7\boldsymbol{T} = {}^4_5\boldsymbol{T}{}^5_6\boldsymbol{T}{}^6_7\boldsymbol{T} = \begin{bmatrix} {}^4_7\boldsymbol{R} & \boldsymbol{n}_{74} \\ 0 & 1 \end{bmatrix} \\ {}^4_8\boldsymbol{T} = {}^4_5\boldsymbol{T}{}^5_6\boldsymbol{T}{}^6_7\boldsymbol{T}{}^7_8\boldsymbol{T} = \begin{bmatrix} {}^4_8\boldsymbol{R} & \boldsymbol{n}_{84} \\ 0 & 1 \end{bmatrix} \end{cases} \tag{1}$$

https://doi.org/10.1017/S0263574721001594 Published online by Cambridge University Press

where ${}_i^j\boldsymbol{T}$ and ${}_i^j\boldsymbol{R}$ $(i, j = 4, 5, 6, 7, 8)$ are the transformation matrix and attitude matrix of the coordinate system i relative to the coordinate system j, and i and j indicate the subscripts of the axes of the coordinate systems; and $\boldsymbol{n}_{ij}$ is the coordinate origin vector of the coordinate system i in the conjoined coordinate system {A-$x_4y_4z_4$}.

The attitude matrix is rewritten as ${}_i^j\boldsymbol{R} = [\boldsymbol{e}_{xij}\ \boldsymbol{e}_{yij}\ \boldsymbol{e}_{zij}]$, and $\boldsymbol{e}_{xij}$, $\boldsymbol{e}_{yij}$, and $\boldsymbol{e}_{zij}$ are the unit direction vectors for the x_i-axis, y_i-axis and z_i-axis, and we can obtain:

$$\begin{cases} \boldsymbol{e}_{kij} = {}_i^j\boldsymbol{R}\boldsymbol{e}_{kii} \\ {}_i^0\boldsymbol{R} = {}_4^0\boldsymbol{R}\,{}_i^4\boldsymbol{R} \end{cases} (i = 5, 6, 7, 8, k = x, y, z) \tag{2}$$

where $e_{xii} = [1\ 0\ 0]^T$, $e_{yii} = [0\ 1\ 0]^T$ and $e_{zii} = [0\ 0\ 1]^T$, ${}_4^0R$ is the attitude matrix of the coordinate system {A-$x_4y_4z_4$} relative to the base coordinate system {B-xyz}.

Based on the principle of angular velocity superposition, the angular velocities of the first joint, the second joint, the orbital motion component, and the rotational motion component are denoted as:

$$\begin{cases} \boldsymbol{\omega}_{fir} = \boldsymbol{\omega}_{40} + \dot{\theta}_5\boldsymbol{e}_{z50} \\ \boldsymbol{\omega}_{sec} = \boldsymbol{\omega}_{40} + \dot{\theta}_5\boldsymbol{e}_{z50} + \dot{\theta}_6\boldsymbol{e}_{z60} \\ \boldsymbol{\omega}_{orb} = \boldsymbol{\omega}_{40} + \dot{\theta}_5\boldsymbol{e}_{z50} + \dot{\theta}_6\boldsymbol{e}_{z60} + \dot{\theta}_7\boldsymbol{e}_{z70} \\ \boldsymbol{\omega}_{rot} = \boldsymbol{\omega}_{40} + \dot{\theta}_5\boldsymbol{e}_{z50} + \dot{\theta}_6\boldsymbol{e}_{z60} + \dot{\theta}_7\boldsymbol{e}_{z70} + \dot{\theta}_8\boldsymbol{e}_{z80} \end{cases} \tag{3}$$

where $\boldsymbol{\omega}_{40}$ is the angular velocity of the moving platform in the base coordinate system, and $\boldsymbol{e}_{zi0}$ (i=5, 6, 7, 8) is the unit direction vector in the corresponding conjoined coordinate system. Further, the angular acceleration of each component for the serial component can be obtained by deriving Eq. (3).

Considering the structure features of 2R series rotary joints and dual rotor grinding system, the elastic deformation can be negligible. The grinding tool of the double rotor grinding system is supplied with output pressure to polish the optical mirror surface by two low friction cylinders, while the output pressure is a constant related to the polishing process. The load acting on 3UPS/UP PM by the serial component can be converted into the equivalent force and moment. Based on the Newton–Euler method, the equivalent force is the sum of the polishing force and the gravity of each component, and the equivalent moment is the sum of the moments produced by the gravity of each component, the polishing force and the inertia force of each component. The equivalent load can be expressed as:

$$\begin{cases} \boldsymbol{F}_{ser} = \boldsymbol{F}_{gri} + (\mathrm{m}_{rot} + \mathrm{m}_{orb} + \mathrm{m}_{sec} + \mathrm{m}_{fir})\boldsymbol{g} \\ \boldsymbol{F}_{gri} = -P_{gri}\left(\dfrac{\pi D_{tool}^2}{4}\right)\boldsymbol{e}_{z80} \end{cases} \tag{4}$$

$$\begin{cases} \boldsymbol{M}_{ser} = \boldsymbol{M}_{gri} + \boldsymbol{M}_g + \boldsymbol{M}_I \\ \boldsymbol{M}_{gri} = {}_4^0\boldsymbol{R}({}_8^4\boldsymbol{R}\boldsymbol{D}_8 + \boldsymbol{n}_{84}) \times \boldsymbol{F}_{gri} \\ \boldsymbol{M}_g = {}_4^0\boldsymbol{R}({}_8^4\boldsymbol{R}\boldsymbol{d}_{crot} + \boldsymbol{n}_{84}) \times (\mathrm{m}_{rot}\boldsymbol{g}) + {}_4^0\boldsymbol{R}({}_7^4\boldsymbol{R}\boldsymbol{d}_{corb} + \boldsymbol{n}_{74}) \times (\mathrm{m}_{orb}\boldsymbol{g}) \\ \qquad + {}_4^0\boldsymbol{R}({}_6^4\boldsymbol{R}\boldsymbol{d}_{csec} + \boldsymbol{n}_{64}) \times (\mathrm{m}_{sec}\boldsymbol{g}) + {}_4^0\boldsymbol{R}({}_5^4\boldsymbol{R}\boldsymbol{d}_{cfir} + \boldsymbol{n}_{54}) \times (\mathrm{m}_{fir}\boldsymbol{g}) \\ \boldsymbol{M}_I = \boldsymbol{I}_{rot0}\boldsymbol{\varepsilon}_{rot} + \boldsymbol{\omega}_{rot} \times \boldsymbol{I}_{rot0}\boldsymbol{\omega}_{rot} + \boldsymbol{I}_{orb0}\boldsymbol{\varepsilon}_{orb} + \boldsymbol{\omega}_{orb} \times \boldsymbol{I}_{orb0}\boldsymbol{\omega}_{orb} \\ \qquad + \boldsymbol{I}_{sec0}\boldsymbol{\varepsilon}_{sec} + \boldsymbol{\omega}_{sec} \times \boldsymbol{I}_{sec0}\boldsymbol{\omega}_{sec} + \boldsymbol{I}_{fir0}\boldsymbol{\varepsilon}_{fir} + \boldsymbol{\omega}_{fir} \times \boldsymbol{I}_{fir0}\boldsymbol{\omega}_{fir} \end{cases} \tag{5}$$

where $\boldsymbol{F}_{gri}$ is the polishing force, m_{rot}, m_{orb}, m_{sec}, and m_{fir} (ϵ_{rot}, ϵ_{orb}, ϵ_{sec}, and ϵ_{fir}) are the masses (angular accelerations) of the rotational motion component, orbital motion component, second joint and first joint, $\boldsymbol{g}$ is the gravity acceleration vector, P_{gri} is the polishing output pressure, D_{tool} is the diameter of the grinding tool, $\boldsymbol{D}_8$ is the coordinate vector of point N in the conjoined coordinate system {A-$x_4y_4z_4$}, $\boldsymbol{d}_{crot}$, $\boldsymbol{d}_{corb}$, $\boldsymbol{d}_{csec}$, and $\boldsymbol{d}_{cfir}$ are the coordinate vectors of the centroid of each component, and $\boldsymbol{I}_{rot0}$, $\boldsymbol{I}_{orb0}$, $\boldsymbol{I}_{sec0}$, and $\boldsymbol{I}_{fir0}$ are the inertia matrices of each component in the base coordinate system.

https://doi.org/10.1017/S0263574721001594 Published online by Cambridge University Press

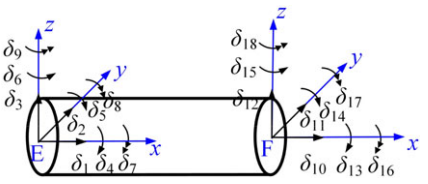

Figure 3. *Diagram of beam element generalized coordinates.*

4. Rigid–Flexible Coupling Dynamic Model of PM

The PM of the polishing robot consists of three UPS branched-chains and a UP branched-chain, and the UPS branched-chains have the same structural parameters. In the rigid–flexible coupling dynamic modeling, there are the following assumptions: (1) The static platform and moving platform are considered as the rigid body; (2) The actual motion of the polishing robot is a linear superposition of rigid and elastic motions, ignoring the coupling term. The rigid–flexible coupling dynamic model of PM is analyzed with Kineto-elasto dynamics method.

4.1. Element dynamic model

The rods in the UPS branched-chains and UP branched-chain are considered to be elastomers. The beam element containing two nodes is selected as the basic elastic model and the diagram is shown in Fig. 3, and 18 generalized coordinates are used to describe the elastic displacements. δ_1–δ_3 and δ_{10}–δ_{12} are the elastic linear displacements at the nodes of the beam element, δ_4–δ_6 and δ_{13}–δ_{15} are the elastic angular displacements, and δ_7–δ_9 and δ_{16}–δ_{18} are the elastic curvatures. The dynamic model of the beam element can be obtained from Lagrange equation:

$$\begin{cases} \boldsymbol{M}_0\ddot{\boldsymbol{\delta}} + \boldsymbol{K}_0\boldsymbol{\delta} = \boldsymbol{F}_0 + \boldsymbol{N}_0 + \boldsymbol{G}_0 \\ \boldsymbol{G}_0 = -\boldsymbol{M}_0\ddot{\boldsymbol{\delta}}_r \end{cases} \tag{6}$$

where $\boldsymbol{M}_0$ is the element mass matrix, $\boldsymbol{K}_0$ is the element stiffness matrix, $\boldsymbol{F}_0$ is the external load matrix, $\boldsymbol{N}_0$ is the load matrix of other elements on the beam element, $\boldsymbol{G}_0$ is the inertial matrix, and $\ddot{\boldsymbol{\delta}}_r$ is the element acceleration array.

4.2. Rigid–flexible coupling dynamic model of branched-chains

According to the structural characteristics of the UPS branched-chain, the branched-chain $B_iC_iD_iA_i$ ($i = 1, 2, 3$) can be divided into three beam elements, and the generalized coordinates in the element coordinate system and base coordinate system are shown in Fig. 4. The prismatic joint C_i can be considered as a rigid connection to eliminate the degree of freedom, and the branched-chain can be regarded as an "instantaneous structure". There are 12 non-zero coordinates in the element B_iC_i. The node D_i is a rotating joint connection point of the composite spherical joint, the elastic curvature along the axis is zero, hence there are 17 non-zero coordinates in the element C_iD_i. Both ends of the element D_iA_i are rotating joints, and there are 14 non-zero coordinates.

The attitude matrix of the element coordinate system $\{B_i\text{-}u_iv_iw_i\}$ relative to the base coordinate system $\{B\text{-}xyz\}$ can be obtained by rotating Ψ_i around the y-axis and then rotating Φ_i around the u_i-axis. And the attitude transformation matrix is orthogonal, so we can obtain:

$${}_0^i\boldsymbol{R} = {}_i^0\boldsymbol{R}^{-1} = {}_i^0\boldsymbol{R}^{\mathrm{T}} = \begin{bmatrix} c\psi_i & s\varphi_i s\psi_i & c\varphi_i s\varphi_i \\ 0 & c\varphi_i & -s\varphi_i \\ -s\psi_i & s\varphi_i c\psi_i & c\varphi_i c\psi_i \end{bmatrix} \tag{7}$$

Since node C_i is assumed to be a rigid connection, the coordinates of the two elements at this node are the same. The node D_i belongs to two elements, thus the elastic displacements of the two elements are

https://doi.org/10.1017/S0263574721001594 Published online by Cambridge University Press

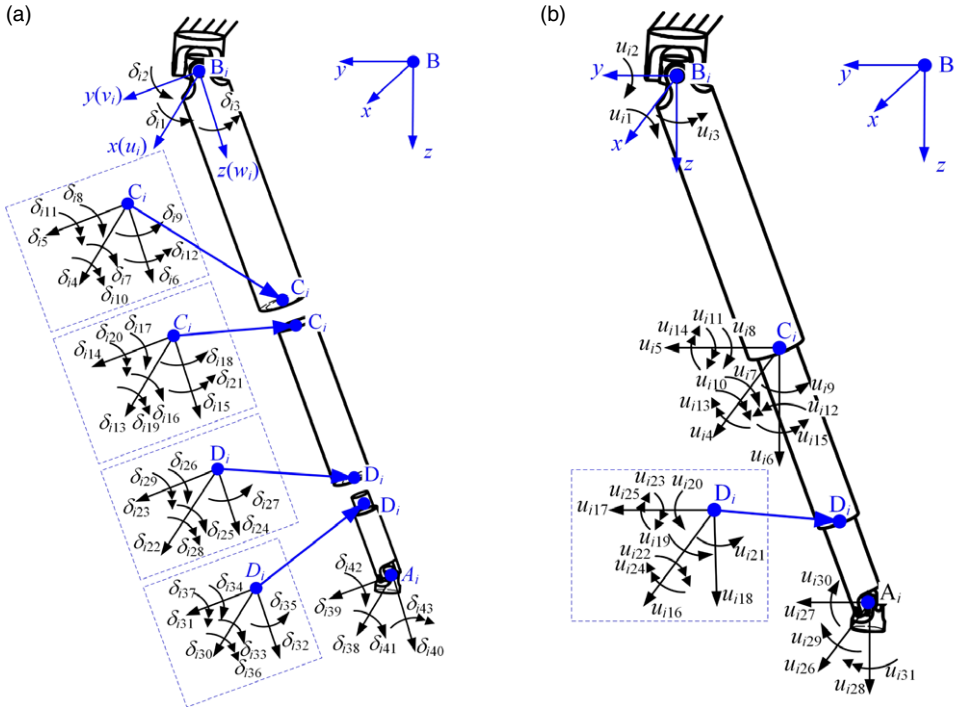

Figure 4. *Generalized coordinates of UPS branched-chain: (a) in element coordinate system, (b) in base coordinate system.*

the same, but the angular displacements and curvatures are different in the base coordinate system. The elastic deformation of UPS branched-chain can be expressed by 43 non-zero coordinates in the element coordinate system and $\boldsymbol{\delta}_{\mathrm{A}_i\mathrm{B}_i} = [\delta_{i1}, \delta_{i2}, \cdots, \delta_{i43}]^{\mathrm{T}}$, and 31 non-zero coordinates in the base coordinate system and $\boldsymbol{U}_i = [u_{i1}, u_{i2}, \cdots, u_{i31}]^T$. And the following correspondence exists:

$$\boldsymbol{\delta}_{\mathrm{A}_i\mathrm{B}_i} = \boldsymbol{B}_i \boldsymbol{U}_i \tag{8}$$

$$\boldsymbol{B}_i = \begin{bmatrix} \boldsymbol{R}^*_{i1} & & & & & & & & & & & & & & & & & & & & & & & & & & & & & & & & \\ & \boldsymbol{R}^*_{i2} & & & & & & & & & & & & & & & & & & & & & & & & & & & & & & \\ & & {}^{i}_{0}\boldsymbol{R} & & & & & & & & & & & & & & & & & & & & & & & & & & & & & \\ & & & {}^{i}_{0}\boldsymbol{R} & & & & & & & & & & & & & & & & & & & & & & & & & & & & & \\ & & & & {}^{i}_{0}\boldsymbol{R} & & & & & & & & & & & & & & & & & & & & & & & & & & & & \\ & & {}^{i}_{0}\boldsymbol{R} & & & & & & & & & & & & & & & & & & & & & & & & & & & & & \\ & & & {}^{i}_{0}\boldsymbol{R} & & & & & & & & & & & & & & & & & & & & & & & & & & & & & \\ & & & & & {}^{i}_{0}\boldsymbol{R} & & & & & & & & & & & & & & & & & & & & & & & & & & & & \\ & & & & & & {}^{i}_{0}\boldsymbol{R} & & & & & & & & & & & & & & & & & & & & & & & & & & & \\ & & & & & & & {}^{i}_{0}\boldsymbol{R} & & & & & & & & & & & & & & & & & & & & & & & & & & \\ & & & & & & & & \boldsymbol{R}^*_{i2} & & & & & & & & & & & & & & & & & & & & & & & & & \\ & & & & & & & {}^{i}_{0}\boldsymbol{R} & & & & & & & & & & & & & & & & & & & & & & & & & & \\ & & & & & & & & {}^{i}_{0}\boldsymbol{R} & & & & & & & & & & & & & & & & & & & & & & & & & \\ & & & & & & & & & \boldsymbol{R}^*_{i2} & & & & & & & & & & & & & & & & & & & & & & & & \\ & & & & & & & & & & {}^{i}_{0}\boldsymbol{R} & & & & & & & & & & & & & & & & & & & & & & & \\ & & & & & & & & & & & \boldsymbol{R}^*_{i2} & & & & & & & & & & & & & & & & & & & & & & \\ & & & & & & & & & & & & \boldsymbol{R}^*_{i1} & & & & & & & & & & & & & & & & & & & & & \end{bmatrix}_{43\times 31}$$

where $\boldsymbol{R}^*_{i1} = \begin{bmatrix} c\phi_i & s\varphi_i s\phi_i \\ 0 & c\varphi_i \end{bmatrix}$ and $\boldsymbol{R}^*_{i2} = c\varphi_i c\phi_i$.

https://doi.org/10.1017/S0263574721001594 Published online by Cambridge University Press

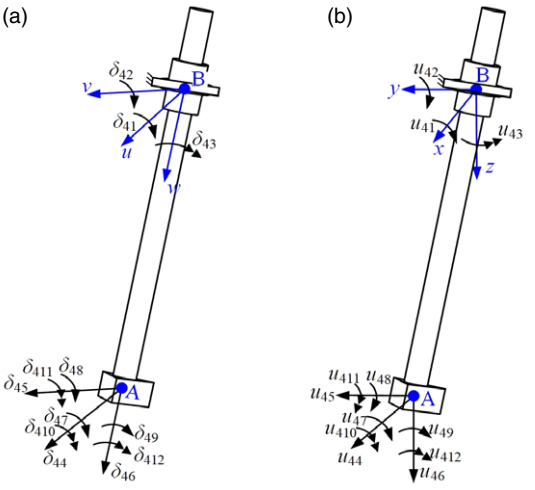

Figure 5. *Generalized coordinates of UP branched-chain: (a) in element coordinate system, (b) in base coordinate system.*

The UP branched-chain BA is connected with the static platform by a Hooke joint, which can be regarded as a beam element. The generalized coordinates in the element coordinate system and base coordinate system are shown in Fig. 5. The Hooke joint consists of a combination of two rotating joints with mutually perpendicular axes, so the elastic curvatures in these two directions are zero. Point B is the connection point between UP branched-chain and the static platform, the elastic linear displacements and elastic angular displacement around the axis are zero, and there are 12 non-zero generalized coordinates for the UP branched-chain. Similarly, the attitude matrix from the coordinate system {B-xyz} to the element coordinate system {B-$u_4v_4w_4$} can be written as:

$$ {}^4_0\boldsymbol{R} = {}^0_4\boldsymbol{R}^{-1} = {}^0_4\boldsymbol{R}^T = \begin{bmatrix} c\phi_4 & s\varphi_4 s\phi_4 & c\varphi_4 s\phi_4 \\ 0 & c\varphi_4 & -s\varphi_4 \\ -s\phi_4 & s\varphi_4 c\phi_4 & c\varphi_4 c\phi \end{bmatrix} \tag{9} $$

The nonzero elastic deformation coordinates of UP branched-chain can be expressed as $\boldsymbol{\delta}_4 = [\delta_{41}, \delta_{42}, \cdots, \delta_{412}]^{\mathrm{T}}$ in element coordinate system, and written as $\boldsymbol{U}_4 = [u_{41}, u_{42}, \cdots, u_{412}]^{\mathrm{T}}$ in the base coordinate system. And the mapping can be described as:

$$ \boldsymbol{\delta}_4 = \boldsymbol{B}_4 \boldsymbol{U}_4 \tag{10} $$

$$ \boldsymbol{B}_4 = \mathrm{diag}(\boldsymbol{R}^*_{41}, \boldsymbol{R}^*_{42}, {}^4_0\boldsymbol{R}, {}^4_0\boldsymbol{R}) $$

Where $\boldsymbol{R}^*_{41} = \begin{bmatrix} c\phi_4 & s\varphi_4 s\psi_4 \\ 0 & c\psi_4 \end{bmatrix}$ and $\boldsymbol{R}^*_{42} = c\varphi_4 c\psi_4$.

Based on the dynamic model of the beam element Eq. (6), the dynamic models of elements B_iC_i, C_iD_i and D_iA_i of UPS branched-chain $B_iC_iD_iA_i$ can be obtained. Furthermore, the dynamic model of UPS branched-chain in the base coordinate system {B-xyz} can be expressed as:

$$ \boldsymbol{M}^i \ddot{\boldsymbol{U}}_i + \boldsymbol{K}^i \boldsymbol{U}_i = \boldsymbol{F}^i + \boldsymbol{N}^i + \boldsymbol{G}^i \ \ (i = 1, 2, 3) \tag{11} $$

$$ \boldsymbol{M}^i = \boldsymbol{B}_i^{\mathrm{T}} \boldsymbol{M}_{e0i} \boldsymbol{B}_i, \ \boldsymbol{K}^i = \boldsymbol{B}_i^{\mathrm{T}} \boldsymbol{K}_{e0i} \boldsymbol{B}_i, \ \boldsymbol{G}^i = -\boldsymbol{M}^i \ddot{\boldsymbol{U}}_{ri} $$

where $\boldsymbol{M}^i$, $\boldsymbol{K}^i$, $\boldsymbol{U}_i$, $\boldsymbol{F}^i$, $\boldsymbol{N}^i$, and $\boldsymbol{G}^i$ are the mass matrix, stiffness matrix, elastic deformation generalized coordinates, external load matrix, the load matrix of other elements and inertial force matrix for UPS branched-chain in the base coordinate system; $\boldsymbol{M}_{e0i}$ and $\boldsymbol{K}_{e0i}$ are the mass matrix and stiffness matrix

https://doi.org/10.1017/S0263574721001594 Published online by Cambridge University Press

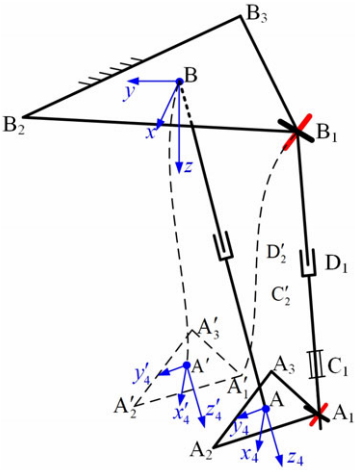

Figure 6. *Position diagram of moving platform considering branched-chains elasticity.*

for UPS branched-chain in element coordinate system; $\ddot{U}_{ri}$ is the rigid body motion acceleration array of UPS branched-chain.

Similarly, the dynamic model of UP branched-chain can be obtained.

4.3. Kinematic constraint of PM

Considering the elastic deformation of branched-chains, the reference point of the moving platform changes from point A to point A', as shown in Fig. 6. The transformation matrix ${}^{0}_{4}\boldsymbol{T}$ from the coordinate system {A-$x_4y_4z_4$} to the coordinate system {B-xyz} can be expressed as:

$$ {}^{0}_{4}\boldsymbol{T} = \begin{bmatrix} {}^{0}_{4}\boldsymbol{R} & r_A \\ 0 & 1 \end{bmatrix}, \quad r_A = (x_{\mathrm{A}}, y_{\mathrm{A}}, z_{\mathrm{A}})^{\mathrm{T}} \tag{12} $$

where $\boldsymbol{r}_{\mathrm{A}}$ is the coordinate vector of point A in the coordinate system {B-xyz}.

The change of position and attitude parameters ($\delta x_{\mathrm{A}}, \delta y_{\mathrm{A}}, \delta z_{\mathrm{A}}, \delta\gamma_{\mathrm{A}}, \delta\beta_{\mathrm{A}}, \delta\alpha_{\mathrm{A}}$) of the moving platform caused by the elastic deformation of the branched-chains tend to zero, and based on Taylor formula and Maclaurin expansion, the coordinate of point A'_i can be expressed as:

$$ \begin{bmatrix} x_{A'_i} \\ y_{A'_i} \\ z_{A'_i} \\ 1 \end{bmatrix} = \Delta\boldsymbol{T} \begin{bmatrix} x_{A_i} \\ y_{A_i} \\ z_{A_i} \\ 1 \end{bmatrix}, \quad \Delta\boldsymbol{T} \approx \begin{bmatrix} 1 & -\delta\alpha_A & \delta\beta_A & \delta x_{\mathrm{A}} \\ \delta\alpha_A & 1 & \delta\gamma_A & \delta y_{\mathrm{A}} \\ -\delta\beta_A & \delta\gamma_A & 1 & \delta z_{\mathrm{A}} \\ 0 & 0 & 0 & 1 \end{bmatrix} \tag{13} $$

The node elastic deformation at point A_i can be expressed as:

$$ \begin{bmatrix} \Delta x_{A_i} \\ \Delta y_{A_i} \\ \Delta z_{A_i} \\ 1 \end{bmatrix} = \begin{bmatrix} x_{A'_i} \\ y_{A'_i} \\ z_{A'_i} \\ 1 \end{bmatrix} - \begin{bmatrix} x_{A_i} \\ y_{A_i} \\ z_{A_i} \\ 1 \end{bmatrix} = (\Delta\boldsymbol{T} - \boldsymbol{E}_{4\times4}) \begin{bmatrix} x_{A_i} \\ y_{A_i} \\ z_{A_i} \\ 1 \end{bmatrix} \tag{14} $$

https://doi.org/10.1017/S0263574721001594 Published online by Cambridge University Press

The kinematic constraint between the UPS branched-chain and the moving platform deformation is as follows:

$$\begin{cases} \boldsymbol{U}_{\mathrm{A}_i} = \boldsymbol{J}_i \boldsymbol{U}_{\mathrm{A}} \\ \boldsymbol{J}_i = \begin{bmatrix} 1 & 0 & 0 & 0 & z_{\mathrm{A}_i} & -y_{\mathrm{A}_i} \\ 0 & 1 & 0 & -z_{\mathrm{A}_i} & 0 & x_{\mathrm{A}_i} \\ 0 & 0 & 1 & y_{\mathrm{A}_i} & -x_{\mathrm{A}_i} & 0 \end{bmatrix} \end{cases} \tag{15}$$

Where $\boldsymbol{J}_i$ is the kinematic constraint matrix of PM, $\boldsymbol{U}_{\mathrm{A}_i}$ is the elastic linear displacement vector of the node A_i, and $\boldsymbol{U}_{\mathrm{A}}$ is the elastic displacement of the reference point of the moving platform.

The front end of UP branched-chain is fixedly connected with the moving platform, and the elastic linear displacements and elastic angular displacements of the front-end node for UP branched-chain are the same as those of the moving platform. There is a kinematic constraint as follows:

$$\boldsymbol{U}'_{\mathrm{A}} = \boldsymbol{J}_4 \boldsymbol{U}_{\mathrm{A}}, \ \ \boldsymbol{J}_4 = \mathbf{E}_{6\times 6} \tag{16}$$

where $\boldsymbol{U}_{\mathrm{A}'}$ is the elastic displacement of the front-end node for UP branched-chain.

4.4. Dynamic model of moving platform

The coupling effect of the rigid motion of the moving platform and the elastic motion caused by branched-chains elasticity is not considered, the velocity and acceleration of the reference point for the moving platform in the base coordinate system {B-*xyz*} can be expressed as:

$$\begin{cases} \dot{u}_{\mathrm{A}'} = [\dot{x}_{\mathrm{A}} + \dot{u}_1 \quad \dot{y}_{\mathrm{A}} + \dot{u}_2 \quad \dot{z}_{\mathrm{A}} + \dot{u}_3 \quad \dot{\gamma}_{\mathrm{A}} + \dot{u}_4 \quad \dot{\beta}_{\mathrm{A}} + \dot{u}_5 \quad \dot{\alpha}_{\mathrm{A}} + \dot{u}_6]^T \\ \ddot{u}_{\mathrm{A}'} = [\ddot{x}_{\mathrm{A}} + \ddot{u}_1 \quad \ddot{y}_{\mathrm{A}} + \ddot{u}_2 \quad \ddot{z}_{\mathrm{A}} + \ddot{u}_3 \quad \ddot{\gamma}_{\mathrm{A}} + \ddot{u}_4 \quad \ddot{\beta}_{\mathrm{A}} + \ddot{u}_5 \quad \ddot{\alpha}_{\mathrm{A}} + \ddot{u}_6]^T \end{cases} \tag{17}$$

where $[\dot{x}_{\mathrm{A}}, \dot{y}_{\mathrm{A}}, \dot{z}_{\mathrm{A}}, \dot{\gamma}_{\mathrm{A}}, \dot{\beta}_{\mathrm{A}}, \dot{\alpha}_{\mathrm{A}}]^{\mathrm{T}}$ and $[\ddot{x}_A, \ddot{y}_A, \ddot{z}_A, \ddot{\gamma}_A, \ddot{\beta}_A, \ddot{\alpha}_A]^T$ are the velocity and acceleration of the reference point A when the moving platform is in rigid body motion.

Based on Newton–Euler method, the dynamic model of the moving platforms can be written as:

$$\begin{bmatrix} m_{\mathrm{A}} & 0 & 0 & 0 & 0 & 0 \\ 0 & m_{\mathrm{A}} & 0 & 0 & 0 & 0 \\ 0 & 0 & m_{\mathrm{A}} & 0 & 0 & 0 \\ 0 & 0 & 0 & I_{xx} & I_{xy} & I_{xz} \\ 0 & 0 & 0 & I_{yx} & I_{yy} & I_{yz} \\ 0 & 0 & 0 & I_{zx} & I_{zy} & I_{zz} \end{bmatrix} \begin{bmatrix} \ddot{x}_{\mathrm{A}} + \ddot{u}_1 \\ \ddot{y}_{\mathrm{A}} + \ddot{u}_2 \\ \ddot{z}_{\mathrm{A}} + \ddot{u}_3 \\ \ddot{\gamma}_{\mathrm{A}} + \ddot{u}_4 \\ \ddot{\beta}_{\mathrm{A}} + \ddot{u}_5 \\ \ddot{\alpha}_{\mathrm{A}} + \ddot{u}_6 \end{bmatrix} = \begin{bmatrix} \sum F_{ix} \\ \sum F_{iy} \\ \sum F_{iz} \\ \sum M_{ix} \\ \sum M_{iy} \\ \sum M_{iz} \end{bmatrix} + \begin{bmatrix} \sum F_{Ax} \\ \sum F_{Ay} \\ \sum F_{Az} \\ \sum M_{\mathrm{A}x} \\ \sum M_{\mathrm{A}y} \\ \sum M_{\mathrm{A}z} \end{bmatrix} \tag{18}$$

where m_{A} is the mass of the moving platform; I_{xx}, I_{xy}, . . ., and I_{zz} are the rotational inertia for the moving platform; $\sum F_{ik}$and $\sum M_{ik}$ ($\sum F_{Ak}$ and $\sum M_{Ak}$) ($k = x, y, z$) are the force and moment of the branched-chains acting on the moving platform (the force and moment acting on the moving platform under external loads) along the axis of the base coordinate system.

The external forces and moments of the PM are influenced by 2R series rotary joints and dual rotor grinding system, and we can obtain:

$$\begin{cases} \left[\sum F_{\mathrm{A}x} \quad \sum F_{\mathrm{A}y} \quad \sum F_{\mathrm{A}z}\right]^{\mathrm{T}} = \boldsymbol{F}_{ser} \\ [\sum M_{\mathrm{A}x} \quad \sum M_{\mathrm{A}y} \quad \sum M_{\mathrm{A}z}]^{\mathrm{T}} = \boldsymbol{M}_{ser} \end{cases} \tag{19}$$

https://doi.org/10.1017/S0263574721001594 Published online by Cambridge University Press

The dynamic model of the moving platform can be rewritten as:

$$\begin{cases} \boldsymbol{M}_{\mathrm{A}}\ddot{\boldsymbol{U}}_{\mathrm{A}'} = \boldsymbol{F}_{\mathrm{A}} + \boldsymbol{N}_{\mathrm{A}} + \boldsymbol{G}_0 \\ \boldsymbol{G}_0 = \begin{bmatrix} \mathrm{m}_{\mathrm{A}} g - \mathrm{m}_{\mathrm{A}} a_{\mathrm{A}} \\ -\boldsymbol{I}_{\mathrm{A}}\dot{\boldsymbol{\omega}}_{\mathrm{A}} - \boldsymbol{\omega}_{\mathrm{A}} \times (\boldsymbol{I}_{\mathrm{A}}\boldsymbol{\omega}_{\mathrm{A}}) \end{bmatrix} \end{cases} \tag{20}$$

where $\boldsymbol{M}_{\mathrm{A}}$ is the mass matrix, $\boldsymbol{F}_{\mathrm{A}}$ is the external load matrix, $\boldsymbol{N}_{\mathrm{A}}$ is the load matrix of other elements on the moving platform, and $\boldsymbol{G}_0$ is the inertial matrix.

The generalized coordinates for UPS branched-chain can be rewritten as $\boldsymbol{U}_i^* = [u_{i1}, \cdots, u_{i26}, u_{i30}, u_{i31}, u_1, u_2, u_3, u_4, u_5, u_6]^T$, and the generalized coordinates of UP branched-chain can be rewritten as $\boldsymbol{U}_4^* = [u_{41}, u_{42}, u_{43}, u_{410}, u_{411}, u_{412}, u_1, u_2, u_3, u_4, u_5, u_6]^T$. According to the kinematic constraints Eqs. (15) and (16), we can obtain:

$$\boldsymbol{U}_i = \boldsymbol{R}_i \boldsymbol{U}_i^*, \begin{cases} \boldsymbol{R}_i = \begin{bmatrix} [\mathbf{E}]_{25\times25} & 0 & 0 \\ 0 & 0 & [\boldsymbol{J}_i]_{3\times6} \\ 0 & [\mathbf{E}]_{3\times3} & 0 \end{bmatrix}_{31\times34} \\ \boldsymbol{R}_4 = \begin{bmatrix} [\mathbf{E}]_{3\times3} & 0 & 0 \\ 0 & 0 & [\boldsymbol{J}_i]_{6\times6} \\ 0 & [\boldsymbol{E}]_{3\times3} & 0 \end{bmatrix}_{12\times12} \end{cases} (i = 1, 2, 3) \tag{21}$$

Substituting Eq. (21) into Eq. (20), we can obtain:

$$\boldsymbol{M}^i \boldsymbol{R}_i \ddot{\boldsymbol{U}}_i^* + \boldsymbol{K}^i \boldsymbol{R}_i \boldsymbol{U}_i^* = \boldsymbol{F}^i + \boldsymbol{N}^i + \boldsymbol{G}^i \ (i = 1, 2, 3, 4) \tag{23}$$

Eq. (23) is left multiplied by $\boldsymbol{R}_i^{\mathrm{T}}$, and it can be rewritten as:

$$\boldsymbol{M}_i \ddot{\boldsymbol{U}}_i^* + \boldsymbol{K}_i \boldsymbol{U}_i^* = \boldsymbol{F}_i, \begin{cases} \boldsymbol{M}_i = \boldsymbol{R}_i^{\mathrm{T}} \boldsymbol{M}^i \boldsymbol{R}_i \\ \boldsymbol{K}_i = \boldsymbol{R}_i^{\mathrm{T}} \boldsymbol{K}^i \boldsymbol{R}_i \\ \boldsymbol{F}_i = \boldsymbol{R}_i^T \left(\boldsymbol{F}^i + \boldsymbol{N}^i + \boldsymbol{G}^i \right) \end{cases} (i = 1, 2, 3, 4) \tag{24}$$

Meanwhile, $\boldsymbol{M}_i$, $\boldsymbol{K}_i$, $\boldsymbol{F}_i$, and U_i^* can be decomposed as follows:

$$\boldsymbol{M}_i = \begin{bmatrix} [\boldsymbol{M}_i^{11}]_{28\times28} & [\boldsymbol{M}_i^{12}]_{28\times6} \\ [\boldsymbol{M}_i^{21}]_{6\times28} & [\boldsymbol{M}_i^{22}]_{6\times6} \end{bmatrix} (i = 1, 2, 3), \boldsymbol{M}_4 = \begin{bmatrix} [\boldsymbol{M}_4^{11}]_{6\times6} & [\boldsymbol{M}_4^{12}]_{6\times6} \\ [\boldsymbol{M}_4^{21}]_{6\times6} & [\boldsymbol{M}_4^{22}]_{6\times6} \end{bmatrix}$$

$$\boldsymbol{K}_i = \begin{bmatrix} [\boldsymbol{K}_i^{11}]_{28\times28} & [\boldsymbol{K}_i^{12}]_{28\times6} \\ [\boldsymbol{K}_i^{21}]_{6\times28} & [\boldsymbol{K}_i^{22}]_{6\times6} \end{bmatrix} (i = 1, 2, 3), \boldsymbol{K}_4 = \begin{bmatrix} [\boldsymbol{K}_4^{11}]_{6\times6} & [\boldsymbol{K}_4^{12}]_{6\times6} \\ [\boldsymbol{K}_4^{21}]_{6\times6} & [\boldsymbol{K}_4^{22}]_{6\times6} \end{bmatrix}$$

$$\boldsymbol{F}_i = \begin{bmatrix} [\boldsymbol{F}_1^i]_{28\times1} \\ [\boldsymbol{F}_2^i]_{6\times1} \end{bmatrix} (i = 1, 2, 3), \boldsymbol{F}_4 = \begin{bmatrix} [\boldsymbol{F}_1^i]_{6\times1} \\ [\boldsymbol{F}_2^i]_{6\times1} \end{bmatrix}$$

$$\boldsymbol{U}_i^* = \begin{bmatrix} [\boldsymbol{U}_i]_{28\times1} \\ [\boldsymbol{U}_{\mathrm{A}}]_{6\times1} \end{bmatrix} (i = 1, 2, 3), \boldsymbol{U}_4^* = \begin{bmatrix} [\boldsymbol{U}_1^i]_{6\times1} \\ [\boldsymbol{U}_2^i]_{6\times1} \end{bmatrix}$$

https://doi.org/10.1017/S0263574721001594 Published online by Cambridge University Press

4.5. Rigid–flexible coupling dynamic model of PM

Assembling the dynamic models of the branched-chains and moving platform, the generalized coordinates of the PM can be written as $\boldsymbol{U} = [\boldsymbol{U}_1, \boldsymbol{U}_2, \boldsymbol{U}_3, \boldsymbol{U}_4]^{\mathrm{T}}$, and the rigid–flexible coupling dynamic model can be expressed as follows:

$$\begin{cases} \boldsymbol{M}\ddot{\boldsymbol{U}} + \boldsymbol{K}\boldsymbol{U} = \boldsymbol{F} + \boldsymbol{G} \\ \boldsymbol{G} = -\boldsymbol{M}\ddot{\boldsymbol{U}}_r \end{cases} \tag{25}$$

$$\boldsymbol{M} = \begin{bmatrix} \boldsymbol{M}_1^{11} & & & & & \boldsymbol{M}_1^{12} \\ & \boldsymbol{M}_2^{11} & & & & \boldsymbol{M}_2^{12} \\ & & \boldsymbol{M}_3^{11} & & & \boldsymbol{M}_3^{12} \\ & & & \boldsymbol{M}_4^{11} & & \boldsymbol{M}_4^{12} \\ \boldsymbol{M}_1^{21} & \boldsymbol{M}_2^{21} & \boldsymbol{M}_3^{21} & \boldsymbol{M}_4^{21} & \boldsymbol{M}_{\mathrm{A}} + \boldsymbol{M}_1^{22} + \boldsymbol{M}_2^{22} + \boldsymbol{M}_3^{22} + \boldsymbol{M}_4^{22} \end{bmatrix}$$

$$\boldsymbol{K} = \begin{bmatrix} \boldsymbol{K}_1^{11} & & & & \boldsymbol{K}_1^{12} \\ & \boldsymbol{K}_2^{11} & & & \boldsymbol{K}_2^{12} \\ & & \boldsymbol{K}_3^{11} & & \boldsymbol{K}_3^{12} \\ & & & \boldsymbol{K}_4^{11} & \boldsymbol{K}_4^{12} \\ \boldsymbol{K}_1^{21} & \boldsymbol{K}_2^{21} & \boldsymbol{K}_3^{21} & \boldsymbol{K}_4^{21} & \boldsymbol{K}_1^{22} + \boldsymbol{K}_2^{22} + \boldsymbol{K}_3^{22} + \boldsymbol{K}_4^{22} \end{bmatrix}, \boldsymbol{F} = \begin{bmatrix} [\boldsymbol{F}_1^1]_{28\times1} \\ [\boldsymbol{F}_1^2]_{28\times1} \\ [\boldsymbol{F}_1^3]_{28\times1} \\ [\boldsymbol{F}_1^4]_{6\times1} \end{bmatrix}$$

where $\boldsymbol{M}$ is the total mass matrix of the PM, $\boldsymbol{K}$ is the total stiffness matrix of the PM, $\boldsymbol{F}$ is the generalized force matrix of the PM, and $\ddot{\boldsymbol{U}}_r$ is the acceleration array of the rigid body motion corresponding to the generalized coordinates.

Considering the effect of viscous damping in rigid–flexible coupling dynamics modeling, the dynamic model of PM can be expressed as follows:

$$\begin{cases} \boldsymbol{M}\ddot{\boldsymbol{U}} + \boldsymbol{C}\dot{\boldsymbol{U}} + \boldsymbol{K}\boldsymbol{U} = \boldsymbol{F} + \boldsymbol{G} \\ \boldsymbol{C} = \lambda_1\boldsymbol{M} + \lambda_2\boldsymbol{K} \end{cases} \tag{26}$$

where $\boldsymbol{C}$ is the damping matrix of the PM, $\dot{U}$ is the first derivative of the generalized coordinates, and λ_1 and λ_2 are the Rayleigh damping coefficients.

5. Rigid–Flexible Coupling Dynamic Model with Joint Clearance

5.1. Kinematic analysis with joint clearance

The branched-chains for the PM consist of several Hooke joints and spherical joints, which are composed of rotating bearings. The local coordinate system $\{O_H\text{-}x_Hy_Hz_H\}$ is established in the rotating joint with clearance, as shown in Fig. 7, O_H is the geometric center of the outer ring, x_H-axis is along the radial direction of the rotating joint and z_H-axis along the axial direction of the rotating joint. R_H is the radius of the outer ring with clearance, r_h is the radius of the inner ring with clearance, O_h is the geometric center of the inner ring for the rotating joint, and O_d is the radial center point of the end face for the rotating joint.

During the polishing robot operation, the radial distance between the inner and outer rings of the rotating joint varies continuously due to the clearance. The polishing robot branched-chains contain rotating joints with various size parameters, and only axial motion errors are taken into account. As shown in Fig. 7, the radial clearance error $\mathbf{C}_r$ and the axial clearance error $\mathbf{C}_t$ for the rotating joint can

https://doi.org/10.1017/S0263574721001594 Published online by Cambridge University Press

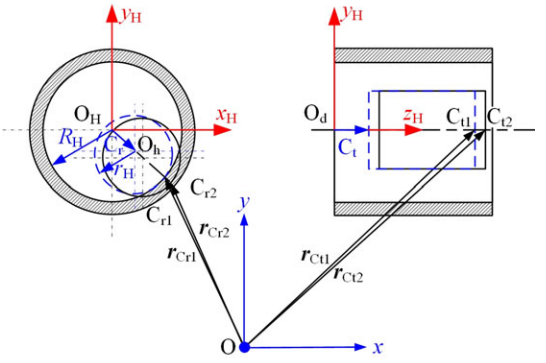

Figure 7. *Structure and collision diagram of rotating joint with clearance.*

be written as follows:

$$\begin{cases} \boldsymbol{C}_{\mathrm{r}} = \delta_{\mathrm{r}} \boldsymbol{n}_{\mathrm{r}} \\ \boldsymbol{C}_{\mathrm{t}} = \delta_{\mathrm{t}} \boldsymbol{n}_{\mathrm{t}} \end{cases} \tag{27}$$

where δ_{r} (δ_{t}) is the radial error (axial error) of the rotating joint when there is no collision, and $\boldsymbol{n}_{\mathrm{r}}$ ($\boldsymbol{n}_{\mathrm{t}}$) is the unit direction vector of radial vibration (axial vibration).

With the changing motion state of the polishing robot, the clearance of the rotating joint shows randomness and uncertainty. In order to reflect the motion state of robot joints more realistically, the joint clearance can be described statistically and considered to follow a normal distribution. The probability density functions of the radial clearance and axial clearance can be expressed as:

$$\begin{cases} f_{\mathrm{r}}(x_{\mathrm{H}}, y_{\mathrm{H}}) = \begin{cases} \dfrac{1}{\sqrt{2\pi}\sigma_{\mathrm{r}}} e^{\kappa r} & 0 \le x_{\mathrm{H}}^2 + y_{\mathrm{H}}^2 \le \delta_{\mathrm{rm}}^2 \\ 0 & \text{other} \end{cases} \\ f_t(z_{\mathrm{H}}) = \begin{cases} \dfrac{1}{\sqrt{2\pi}\sigma_t} e^{\kappa t} & 0 \le z_{\mathrm{H}} \le \delta_{\mathrm{tm}} \\ 0 & \text{other} \end{cases} \end{cases} \tag{28}$$

where $\kappa \mathrm{r} = \left(\frac{\sqrt{x_H^2 + y_H^2} - \mu_{\mathrm{r}}}{\sqrt{2}\sigma_{\mathrm{r}}} \right)^2$ and $\kappa \mathrm{t} = \left(\frac{z_{\mathrm{H}} - \mu_t}{\sqrt{2}\sigma_{\mathrm{t}}} \right)^2$; δ_{rm} is the maximum value of the radial joint clearance without collision and $\delta_{\mathrm{rm}} = R_{\mathrm{H}} - r_{\mathrm{h}}$; δ_{tm} is the maximum value of the axial joint clearance without collision; σ_{r} and σ_{t} (μ_{r} and μ_{t}) are the standard deviation (average value) of the probability density function.

When there is no collision in the rotating joint, the radial clearance δ_{rc} is equal to δ_{r} and the axial clearance δ_{tc} is equal to δ_{t}, δ_{r} and δ_{t} are the mathematical expectation of probability density function for the joint clearance. When there is a collision in the rotating joint, $\delta_{rc} = \delta_{\mathrm{rm}} + \delta_{\mathrm{rf}}$ and $\delta_{\mathrm{tc}} = \delta_{\mathrm{tm}} + \delta_{\mathrm{tf}}$, δ_{rf} and δ_{tf} are the elastic displacements with the joint collision.

The center point of the joint inner ring moves in a cylindrical area with the center point of the joint outer ring as the center and the radius of the maximum distance δ_{rc} between the inner and outer ring axes. The position of any point I of the K+1-th joint connector is shown in Fig. 8. L_{K+1} is the modulus of the vector of the point I in the joint coordinate system, θ_{d1} is the angle between the centerline of the inner ring and outer ring and the x_{H}-axis positive direction, and θ_{d2} is the angle between the K+1-th joint connector and the x_{H}-axis positive direction.

The Hook joints in UPS branched-chains and UP branched-chain can be decomposed into two sets of mutually perpendicular rotating joints, and the composite spherical joints in UPS branched-chains can be decomposed into three sets of mutually vertical rotating joints. And the joint coordinate system with joint clearance is shown in Fig. 9. In the joint coordinate system, the coordinates of the point I of

https://doi.org/10.1017/S0263574721001594 Published online by Cambridge University Press

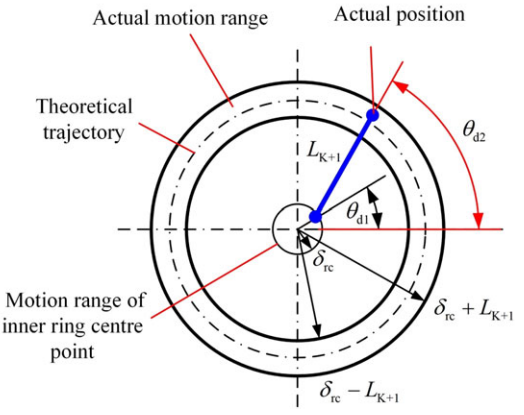

Figure 8. *Diagram of motion position for joint connector.*

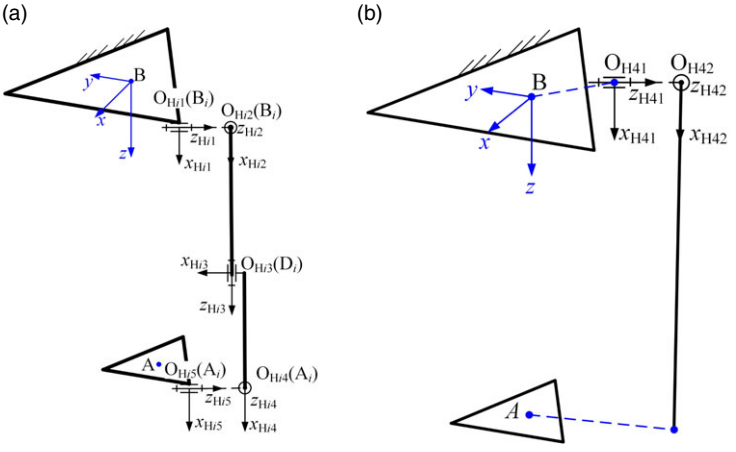

Figure 9. *Diagram of joint coordinate systems: (a) UPS branched-chain, (b) UP branched-chain.*

the $K+1$-th joint connector can be expressed as:

$$\begin{cases} x_I = \delta_{rc} \cos\theta_{d1} + L_{K+1} \cos\theta_{d2} \\ y_I = \delta_{rc} \sin\theta_{d1} + L_{K+1} \sin\theta_{d2} \\ z_I = \delta_{tc} \end{cases} \tag{29}$$

Thus, in the joint coordinate system, considering the joint clearance, the coordinate of any point I of the $K+1$-th joint connector for i-th branched-chain can be expressed as $\boldsymbol{P}_{Hil} = [x_I, y_I, z_I]^T$. The transformation matrix of the j-th rotating joint coordinate system of the i-th branched-chain relative to the base coordinate system is $\boldsymbol{T}_{H0ij}$, thus, the vector of the point I in the $K+1$-th joint connector can be expressed as $\boldsymbol{P}_{H0il} = \boldsymbol{T}_{H0ij}\boldsymbol{P}_{Hil}$.

The joint clearance for the polishing robot is generally small, and the force caused by the speed change is generally small, so only the joint impact force and friction force with the joint clearance are considered, and the diagram of joint collision with clearance is shown in Fig. 7. When the inner and outer of the rotating joint collide with each other, the contact points are C_{r1} and C_{t1}, and the position vectors in the base coordinate system are $\boldsymbol{r}_{Cr1}$ and $\boldsymbol{r}_{Ct1}$, respectively. At the end of the joint collision, the contact points of the joint inner ring are C_{r2} and C_{r2}, and the position vectors in the base coordinate

https://doi.org/10.1017/S0263574721001594 Published online by Cambridge University Press

system are $\boldsymbol{r}_{\mathrm{Cr2}}$ and $\boldsymbol{r}_{\mathrm{Ct2}}$, respectively. And we can obtain:

$$\begin{cases} \boldsymbol{r}_{\mathrm{Cr1}} = \boldsymbol{R}_{\mathrm{OH}} + \boldsymbol{n}_{\mathrm{R}} R_{\mathrm{H}} \\ \boldsymbol{r}_{\mathrm{Cr2}} = \boldsymbol{r}_{\mathrm{Oh}} + \boldsymbol{n}_{\mathrm{R}} r_{\mathrm{h}} \end{cases} \tag{30}$$

When a radial collision occurs between the inner and outer rings for the rotating joint, the normal and tangential velocities can be expressed as:

$$\begin{cases} \boldsymbol{v}_{\mathrm{Hn}} = [(\dot{\boldsymbol{r}}_{\mathrm{Cr1}} - \dot{\boldsymbol{r}}_{\mathrm{Cr2}})^{\mathrm{T}} \boldsymbol{n}_{\mathrm{R}}] \dot{\boldsymbol{n}}_{\mathrm{R}} \\ \boldsymbol{v}_{\mathrm{Ht}} = \dot{\boldsymbol{r}}_{\mathrm{Cr1}} - \dot{\boldsymbol{r}}_{\mathrm{Cr2}} - \boldsymbol{v}_{\mathrm{Hn}} \end{cases} \tag{31}$$

In the same way, when an axial collision occurs, we can obtain:

$$\begin{cases} \boldsymbol{v}_{\mathrm{Hn}} = [(\dot{\boldsymbol{r}}_{\mathrm{Ct1}} - \dot{\boldsymbol{r}}_{\mathrm{Ct2}})^{\mathrm{T}} \boldsymbol{n}_{\mathrm{R}}] \dot{\boldsymbol{n}}_{\mathrm{R}} \\ \boldsymbol{v}_{\mathrm{Ht}} = \dot{\boldsymbol{r}}_{\mathrm{Ct1}} - \dot{\boldsymbol{r}}_{\mathrm{Ct2}} - \boldsymbol{v}_{\mathrm{Hn}} \end{cases} \tag{32}$$

5.2. Joint contact force with clearance

In the polishing process for optical mirrors, the 2R series rotary joints and dual rotor grinding system exert periodic force on the PM. Therefore, the Lankarani–Nikravesh model with a high coefficient of restitution and low energy consumption can be used to represent the contact force.

$$\begin{cases} F_{\mathrm{N}} = K\delta^{1.5} \left(1 + \dfrac{3\left(1 - c^2\right)\dot{\delta}_c}{4\dot{\delta}_0} \right) \\ K = \dfrac{4}{3\left(\delta_1 + \delta_2\right)} \sqrt{\dfrac{r_{\mathrm{H}} R_{\mathrm{H}}}{R_{\mathrm{H}} - r_{\mathrm{H}}}} \end{cases} \tag{33}$$

where K is the stiffness coefficient; c is the restitution coefficient; δ_i (i=1, 2) is the parameter related to the component material; $\delta_i = (1 - v_i^2)/E_i$, v_i and E_i is the Poisson's ratio and elastic modulus; $\dot{\delta}_0$ and $\dot{\delta}_c$ are the collision velocity and relative velocity.

The joint friction can be described with the Coulomb model,

$$\boldsymbol{f}_{\mathrm{H}} = -\mu F_{\mathrm{N}} (\boldsymbol{v}_{\mathrm{Hn}} + \boldsymbol{v}_{\mathrm{Ht}}) \tag{34}$$

where μ is the friction coefficient.

Therefore, the joint contact force with the clearance can be expressed as:

$$\boldsymbol{F}_{\mathrm{H}} = \boldsymbol{n}_{\mathrm{R}} F_{\mathrm{N}} + \boldsymbol{f}_{\mathrm{H}} \tag{35}$$

5.3. Dynamic model of polishing robot with joint clearance

Based on the Jacobian matrix of the PM, the joint contact force $\boldsymbol{F}_{\mathrm{H}}$ with clearance can be transformed into the joint space, and it can be written as:

$$F_{\mathrm{HA}} = J_{\mathrm{H}}^{\mathrm{T}} F_{\mathrm{H}} \tag{36}$$

Substituting Eq. (36) into Eq. (26), the rigid–flexible coupling dynamics of the PM with the joint clearance can be rewritten as:

$$\boldsymbol{M}_{\mathrm{H}} \ddot{U}_H + \boldsymbol{C}_H \dot{U}_H + \boldsymbol{K}_H \boldsymbol{U}_H = \boldsymbol{F}_H + \boldsymbol{G}_H \tag{37}$$

where $\boldsymbol{M}_{\mathrm{H}}$, $\boldsymbol{K}_{\mathrm{H}}$, $\boldsymbol{F}_{\mathrm{H}}$ and $\boldsymbol{G}_{\mathrm{H}}$ are the mass matrix, stiffness matrix, matrix of forces and moments between the elements and matrix of the external force and inertial force for the PM with the joint clearance; $\boldsymbol{U}_{\mathrm{H}}$ is the generalized coordinate vector of the PM in the elastic motion of the branched-chains with the joint clearance, $\dot{\boldsymbol{U}}_{\mathrm{H}}$ and $\ddot{\boldsymbol{U}}_{\mathrm{H}}$ are the generalized velocity vector and generalized acceleration vector of the PM in the elastic motion of the branched-chains with the joint clearance.

https://doi.org/10.1017/S0263574721001594 Published online by Cambridge University Press

Table II. *Structure parameters of polishing robot.*

Parameters	**Value**
Diameter of static platform external circle (m)	0.8
Diameter of moving platform external circle (m)	0.3
Distance between point B and point P d_4 (m)	0.432
Inner/outer diameter of element CD (mm)	45/69
Diameter of element DA (mm)	36
Distance between point P and point H a_6 (m)	0.228
Distance between point H and point N d_7 (m)	0.020
Diameter of grinding tool D_{tool} (mm)	10
Inner/outer diameter of element BC (mm)	92/108
Element density (g·cm^3)	7.9
Polishing output pressure P_{gri} (KPa)	20
Mass of rotational component m_{rot} (Kg)	1.536
Mass of first joint m_{fir} (Kg)	71.661
Mass of orbital component m_{orb} (Kg)	19.015
Mass of second joint m_{sec} (Kg)	45.449
Elastic modulus (Pa)	1.96×10^{11}
Inertia matrix of rotational component (kg·m^2)	diag(0.05,0.05,0)
Inertia matrix of second joint (kg·m^2)	diag(0.802,0.499,1.173)
Inertia matrix of first joint (kg·m^2)	diag(2.085,1.573,1.584)
Inertia matrix of orbital component (kg·m^2)	$\begin{bmatrix} 0.371 & -0.004 & 0.011 \\ -0.004 & 0.481 & 0.010 \\ 0.011 & 0.010 & 0.193 \end{bmatrix}$

Table III. *Dynamics parameters of PM with joint clearance.*

Parameters	**Value**
Restitution coefficient	0.9
Poisson's ratio	0.3
Collision depth (mm)	0.1
Friction coefficient	0.01
Standard deviation of probability function	1
Rayleigh damping coefficient λ_1	2×10^{-3}
Rayleigh damping coefficient λ_2	3×10^{-4}

6. Dynamic Simulation

In the base coordinate system {B-xyz}, the motion trajectory of the moving platform and 2R series rotary joints for the polishing robot is given in Eq. (38) and the units are mm and rad. The angular velocities of the rotational motion and orbital motion for the grinding system during the polishing process of the optical mirror are $\omega_{rot}=14\pi$ rad/s and $\omega_{orb}=12\pi$ rad/s. And the parameters of the polishing robot are shown in Tables II and III.

$$\begin{cases} x = 300\cos(0.01\pi t) \\ y = 300\cos(0.01\pi t) \\ z = 1100 \\ \theta_5 = \pi t/100 \\ \theta_6 = 2(\pi/2 - \operatorname{atan}(1/3))\sin(\pi t/200) \end{cases} \tag{38}$$

https://doi.org/10.1017/S0263574721001594 Published online by Cambridge University Press

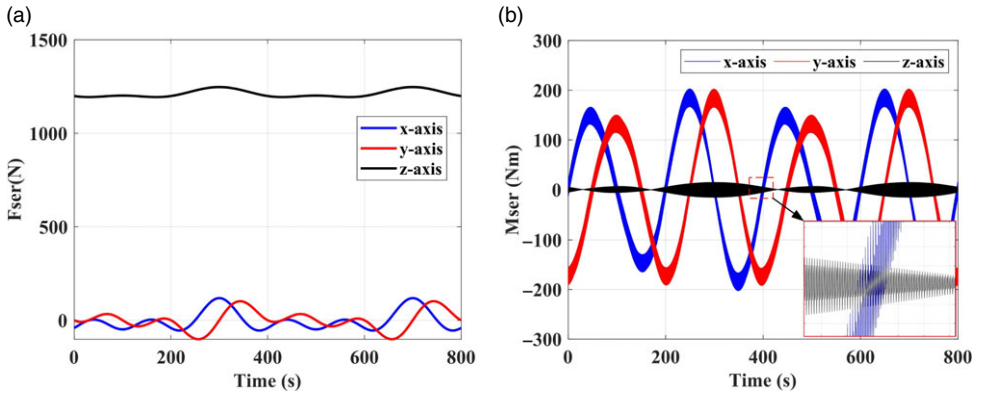

Figure 10. *Equivalent load of PM: (a) equivalent force, (b) equivalent moment.*

The equivalent load of the serial component on the moving platform of the PM is shown in Fig. 10. The reference point of the moving platform moves in a circle at a fixed distance from the static platform, so the forces change with time as a trigonometric function. The equivalent force and moment are mainly from the gravity of the 2R series rotary joints and dual rotor grinding system and polishing force. The rotational and orbital axes are parallel for the grinding system, and the force acting on the PM is not affected by the rotational and orbital motions, but only related to the motion attitude of the PM. Figure 10(a) shows that the equivalent force in the z-axis is much greater than that in the x-axis and y-axis, and the equivalent force with smaller amplitude is mainly produced by the motion of the moving platform and larger amplitude is mainly produced by the motion of the 2R series rotary joints.

The frequency of the rotational and orbital motions for the grinding system is relatively high, thus the equivalent load of the serial component on the PM is mainly in the form of the moment, and the equivalent moment is strip in shape. Figure 10(b) shows that the equivalent moment is the superposition of two trigonometric functions, the larger amplitude of the equivalent moment is mainly affected by the orbital motion and the smaller amplitude is mainly affected by the rotational motion. The equivalent moment components along the x-axis and y-axis have large amplitude variations, while the component along the z-axis is small.

Under the action of the serial component of the polishing robot, the position and angle errors of the moving platform for the PM considering the branched-chains elastic deformation are shown in Fig. 11. Due to the periodic variation of the equivalent force and moment of the serial component on the PM, the motion errors of the PM also present a strip trend. From the local amplification results, it can be seen that the errors are the superposition of two high frequency periodic deformations, the motion error with a smaller amplitude is affected by the rotational motion of the grinding system and the motion error with a larger amplitude is affected by the orbital motion of the grinding system. The position error of the moving platform with the branched-chains elasticity along the x-axis and y-axis varies between ± 0.03 mm and the angle error varies between $\pm 2.74 \times 10^{-5}$ rad. Figure 11(c1) and (c2) show that the position error and the angle error along the z-axis have two different amplitudes, this is due to the periodic motion of the second joint of 2R series rotary joints, and at the boundary of motion space, the force and the moment exerted by the serial component on the PM are different. Besides, the motion period of the second joint is twice that of the PM, thus the error also has different amplitudes. The position error along the z-axis varies from -0.008 to 0.0047 mm, and the angle error varies from -7.45×10^{-7} rad to 6.33×10^{-7} rad. For the polishing robot, the UP branched-chain is fixed to the moving platform and the structure size is large, so the high stiffness of the z-axis leads to less error with the influence of the elastic deformation. Furthermore, the equivalent moment along the z-axis of the serial component is very small, thus the angle error along the z-axis has a small value and presents a straight strip.

To further analyze the influence of the joint clearance on the motion accuracy of the polishing robot, the polishing robot also follows the motion law of Eq. (38). The Hooke joint of branched-chains is

https://doi.org/10.1017/S0263574721001594 Published online by Cambridge University Press

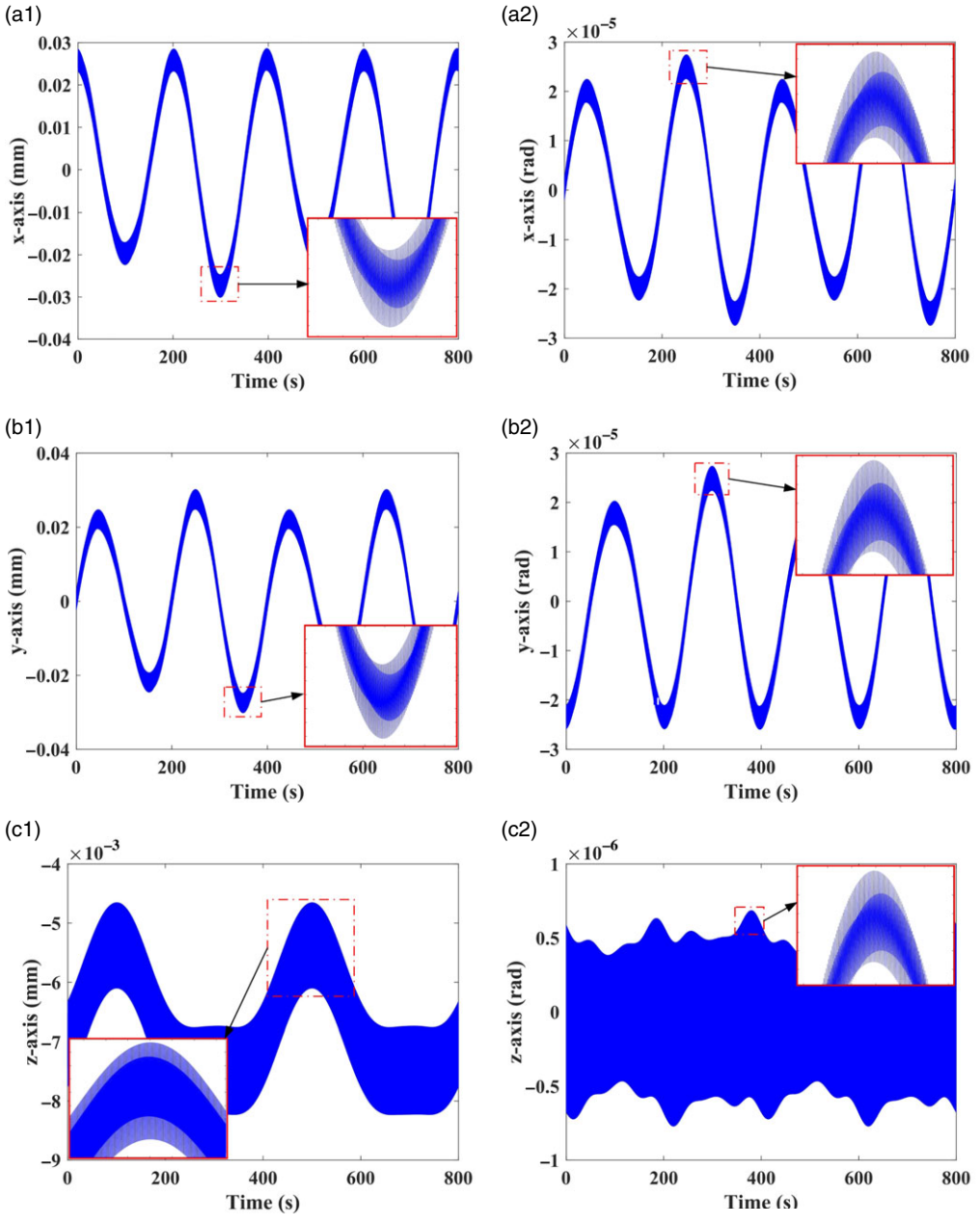

Figure 11. *Motion error of moving platform considering branched-chains elasticity: (a1) position error in x-axis direction, (a2) angle error in x-axis direction, (b1) position error in y-axis direction, (b2) angle error in y-axis direction, (c1) position error in z-axis direction, and (c2) angle error in z-axis direction.*

formed by two sets of rolling bearings with the same structure and vertically intersecting axes, and the composite spherical joint of UPS branched-chains is formed by three sets of rolling bearings with the same structure and vertically intersecting axes. The joint clearance parameters of the branched-chains for the dynamics simulation are shown in Table IV. Taking the first 0.2 s of the simulation motion time, the position error at the reference point of the moving platform is shown in Fig. 12 when only the branched-chain elasticity is considered. The simulation motion time is shorter than that of the polishing

https://doi.org/10.1017/S0263574721001594 Published online by Cambridge University Press

Table IV. *Joint clearance parameters of branched-chains.*

Joint number	$\mathbf{H}_{i1}$	$\mathbf{H}_{i2}$	$\mathbf{H}_{i3}$	$\mathbf{H}_{i4}$	$\mathbf{H}_{i5}$	$\mathbf{H}_{41}$	$\mathbf{H}_{42}$
Radial clearance (mm)	0.05	0.05	0.03	0.03	0.03	0.07	0.07
Axial clearance (mm)	0.04	0.04	0.02	0.03	0.03	0.05	0.05

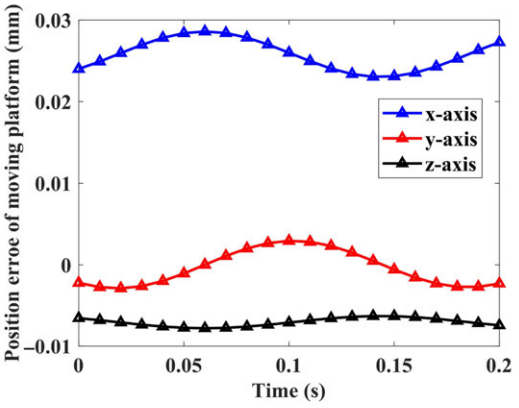

Figure 12. *Motion error of moving platform considering branched-chain elasticity.*

robot, thus there is no periodic amplitude caused by the orbital and rotational motion of the dual rotor grinding system.

When considering the elasticity of the branched-chains and joint clearance, the position error of the moving platform is shown in Fig. 13. Combined with Fig. 12, we find that the position error of the reference point of the moving platform is greatly affected by the elastic deformation of the branched-chains, and the changing trend is similar to that when only considering the elasticity of the branched-chain. The equivalent force and moment of the dual rotor grinding system on the moving platform are larger than the impact force and friction caused by the joint clearance. The joint clearances of the polishing robot lead to a small amplitude oscillation of the error of the moving platform. At the same time, in the simulation time, the equivalent force and moment of the moving platform along the x-axis are relatively large, which leads to the error of the x-axis is larger than that of the y-axis and z-axis.

7. Conclusion

This article proposes a hybrid polishing robot consisting of a 3-DOF PM, 2R series rotary joints and a dual rotor grinding system with high polishing accuracy, compactness and stiffness to comply with the trend of high precision operation of optical mirrors.

(1) Based on the kinematics of the 2R series rotary joints and dual rotor grinding system of the polishing robot, the equivalent load model of the serial components on the PM is established. The results show that the equivalent force is mainly distributed along z-axis, and the equivalent moment is mainly distributed in x-axis and y-axis and consists of the superposition of two trigonometric functions.

(2) Based on the rigid–flexible coupling dynamic model of the PM, the elasticity of the branched-chains mainly leads to motion errors of the moving platform in x-axis and y-axis and the robot is more resistant to deformation in z-axis. Due to the high-frequency motion of the grinding system, the motion errors of the moving platform have a striped distribution in all directions.

https://doi.org/10.1017/S0263574721001594 Published online by Cambridge University Press

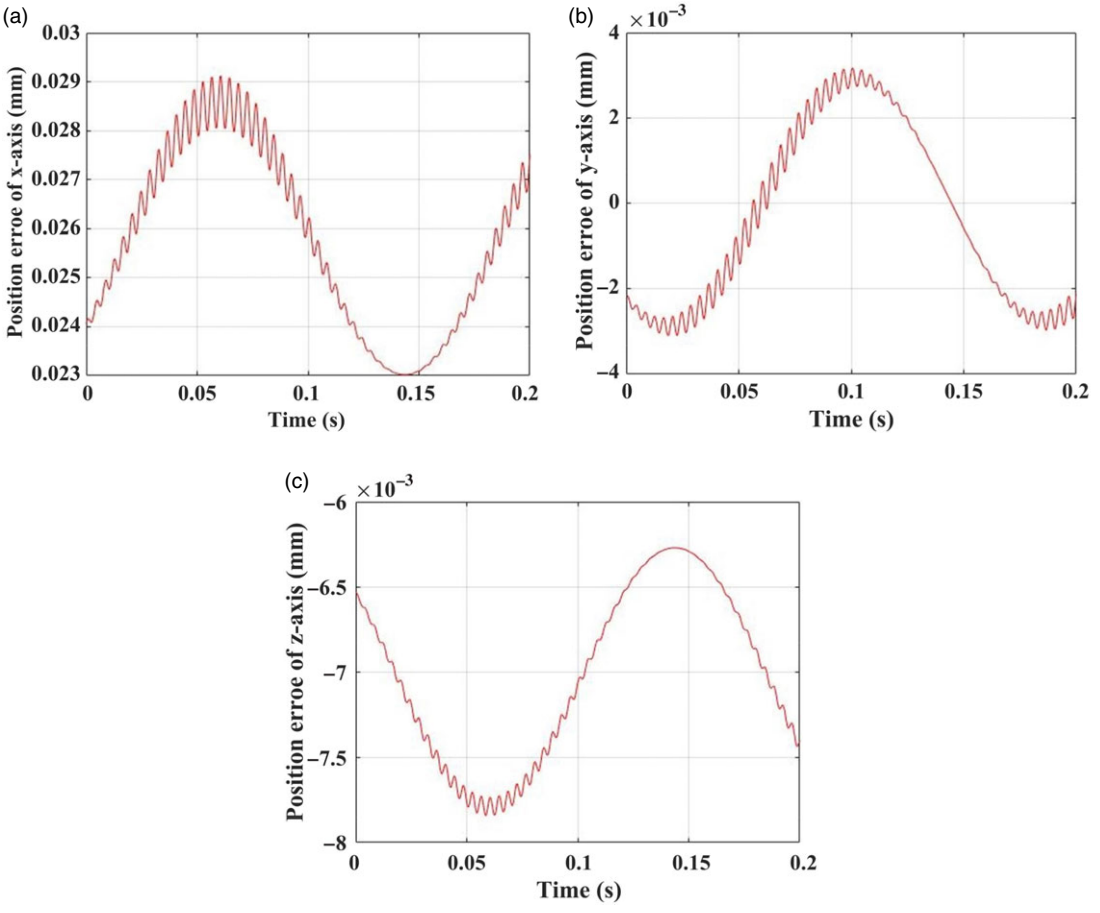

Figure 13. *Motion error of moving platform considering branched-chain elasticity and joint clearance: (a) x-axis, (b) y-axis, (c) z-axis.*

(3) When the joint clearance is considered in the rigid–flexible coupling dynamics, the motion errors of the PM moving platform considering both joint clearance and branched-chain elasticity have a local runout compared with the motion errors considering only the branched-chain elasticity.

The analysis of rigid–flexible coupling dynamics of the polishing robot including the branched-chain elasticity and joint clearance provides a theoretical basis for improving the motion accuracy and dynamic characteristics of the polishing robot.

Acknowledgments. Financial support for this work, provided by the Priority Academic Program Development of Jiangsu Higher Education Institutions and the National Natural Science Foundation of China (Grant No. 91648105), is gratefully acknowledged.

Conflict of Interest. The authors declare that they have no competing interests.

References

1. S. Canfield, J. Owens and S. Zuccaro, "Zero moment control for lead-through teach programming and process monitoring of a collaborative welding robot," *J. Mech. Robot.* **13**(3), 031114 (2021).
2. M. Zhou, Q. Yu, K. Huang, S. Mahov, A. Eslami, M. Maier, C. Lohmann, N. Navab, D. Zapp, A. Knoll and M. Nasseri, "Towards robotic-assisted subretinal injection: A hybrid parallel-serial robot system design and preliminary evaluation," *IEEE T. Ind. Electron.* **67**(8), 6617–6628 (2020).

https://doi.org/10.1017/S0263574721001594 Published online by Cambridge University Press

3. S. Pellegrinelli, N. Pedrocchi, L. Tosatti, A. Fischer and T. Tolio, "Multi-robot spot-welding cells for car-body assembly: Design and motion planning," *Robot. Cim. -Int. Manuf.* **44**, 97–116 (2017).
4. B. Li, Y. Li and X. Zhao, "Kinematics analysis of a novel over-constrained three degree-of-freedom spatial parallel manipulator. *Mech. Mach. Theory* **104**, 222–233 (2016).
5. N. Plitea, A. Szilaghyi and D. Pisla, "Kinematic analysis of a new 5-DOF modular parallel robot for brachytherapy," *Robot. Cim.-Int. Manuf.* **31**, 70–80 (2015).
6. W. Lin, B. Li, X. Yang and D. Zhang, "Modelling and control of inverse dynamics for a 5-DOF parallel kinematic polishing machine," *Int. J. Adv. Robot. Syst.* **10**(13), 1–21 (2013).
7. P. Xu, C. Cheung, B. Li, L. Ho and J. Zhang, "Kinematics analysis of a hybrid manipulator for computer controlled ultra-precision freeform polishing," *Robot. Cim. -Int. Manuf.* **44**, 44–56 (2017).
8. X. Yang, H. Liu, J. Xiao, W. Zhu, Q. Liu, G. Gong and T. Huang, "Continuous friction feedforward sliding mode controller for a TriMule hybrid robot," *IEEE-ASME Trans. Mechatron*. **23**(4), 1673–1683 (2018).
9. C. Dong, H. Liu, W. Yue and T. Huang, "Stiffness modeling and analysis of a novel 5-DOF hybrid robot," *Mech. Mach. Theory.* **125**, 80–93 (2018).
10. Y. Xu, Z. Teng, J. Yao, Y. Zhou and Y. Zhao, "Elastodynamic analysis of a novel motion-decoupling forging manipulator," *Mech. Mach. Theory* **147**, 103771 (2020).
11. A. Chebbi, Z. Affi and L. Romdhane, "Prediction of the pose errors produced by joints clearance for a 3-UPU parallel robot," *Mech. Mach. Theory* **44**(9), 1768–1783 (2009).
12. Y. Jiang, T. Li and L. Wang, "Dynamic modeling and redundant force optimization of a 2-DOF parallel kinematic machine with kinematic redundancy," *Robot. Cim. -Int. Manuf.* **32**, 1–10 (2015).
13. S. Mousavi, V. Gagnol, B. Bouzgarrou and P. Ray, "Stability optimization in robotic milling through the control of functional redundancies," *Robot. Cim. -Int. Manuf.* **50**, 181–192 (2018).
14. Z. Xie, F. Xie, X. Liu, J. Wang and X. Shen, "Parameter optimization for the driving system of a 5-DOF parallel machining robot with planar kinematic chains," *J. Mech. Robot.* **11**(4), 1–17 (2019).
15. Z. Liu, X. Tang, Z. Shao and L. Wang, "Dimensional optimization of the Stewart platform based on inertia decoupling characteristic," *Robotica* **34**(5), 1151–1167 (2016).
16. X. Shan and G. Cheng, "Structural error and friction compensation control of a 2(3PUS+S) parallel manipulator," *Mech. Mach. Theory* **124**, 92–103 (2018).
17. F. Guo, G. Cheng and Y. Pang, "Explicit dynamic modeling with joint friction and coupling analysis of a 5-DOF hybrid polishing robot," *Mech. Mach. Theory* **167**, 104509 (2022).
18. G. Wu, S. Caro, S. Bai and J. Kepler, "Dynamic modeling and design optimization of a 3-DOF spherical parallel manipulator," *Robot. Auton. Syst.* **62**(10), 1377–1386 (2014).
19. B. Hu and J. Yu, "Unified solving inverse dynamics of 6-DOF serial-parallel manipulators," *Appl. Math. Model.* **39**(16), 4715–4732 (2015).
20. J. Liu, Y. Li, Y. Zhang, Q. Gao and B. Zuo, "Dynamics and control of a parallel manipulator for active vibration isolation in space station," *Nonlinear Dyn.* **76**(3), 1737–1751 (2014).
21. C. Dong, H. Liu, T. Huang and D. Chetwynd, "A screw theory based semi-analytical approach for elastodynamics of the Tricept robot," *J. Mech. Robot.* **11**(3), 031005 (2019)
22. A. Cammarata, "Full and reduced models for the elastodynamics of fully flexible parallel robots," *Mech. Mach. Theory* **151**, 103895 (2020).
23. C. Alessandro and S. Rosario, "Elastodynamic optimization of a 3T1R parallel manipulator," *Mech. Mach. Theory* **73**(73), 184–196 (2014).
24. P. Flores, M. Machado, M. Silva and J. Martins, "On the continuous contact force models for soft materials in multi-body dynamics," *Multibody Syst. Dyn.* **25**(3), 357–375 (2011).
25. S. Mukras, N. Kim and N. Mauntler, "Analysis of planar multibody systems with revolute joint wear," *Wear* **268**(5), 643–652 (2010).
26. Z. Wang, Q. Tian, H. Hu and P. Flores, "Nonlinear dynamics and chaotic control of a flexible multibody system with uncertain joint clearance," *Nonlinear Dynam.* **86**(3), 1571–1597 (2016).
27. X. Chen, W. Gao, Y. Deng and Q. Wang, "Chaotic characteristic analysis of spatial parallel manipulator with clearance in spherical joint," *Nonlinear Dynam.* **94**(4), 2625–2642 (2018).
28. S. Varedi-Koulaei, H. Daniali and M. Farajtabar, "The effects of joint clearance on the dynamics of the 3RRR planar parallel manipulator," *Robotica* **35**(6), 1223–1242 (2016).
29. B. Xu, X. Wang, X. Ji, R. Tong and Y. Xue, "Dynamic and motion consistency analysis for a planar parallel manipulator with revolute dry clearance joints," *J. Mech. Sci. Technol.* **31**(7), 3199–3209 (2017).

Cite this article: F. Guo, G. Cheng, S. Wang and J. Li (2022). "Rigid–flexible coupling dynamics analysis with joint clearance for a 5-DOF hybrid polishing robot", Robotica **40**, 2168–2188. https://doi.org/10.1017/S0263574721001594